BIOMECHANICAL ANALYSIS OF HARD TISSUE RESPONSES AND INJURIES WITH FINITE ELEMENT FULL HUMAN BODY MODEL

Jay Zhijian Zhao, Gopal Narwani
TK Holdings Inc.
United States
Paper Number 07-0354

ABSTRACT

This paper summarizes the development activities on the finite element full human body model, improving upon last 19th ESV publication (ESV 05-0399). The updated Takata Human Model for an average adult male has anatomical details of skeleton and major soft tissues in all the body parts—head, neck, shoulder, thorax, abdomen, pelvis, lower and upper extremities. The arteries and veins as well as sciatic nerves in pelvis, thigh and tibia regions were also modeled. The model's responses of all the body parts were validated against published or in-house PMHS test data of twenty tissue material tests and forty-seven pendulum, drop or sled tests under frontal, side and oblique and rear impacts. A method similar to those defined in the ISO-TR9790 lateral biofidelity rating procedures was applied for evaluation of the model biofidelity. The overall biofidelity rating of the model is good (8.1).

Biomechanical analysis using this model has been made on fractures of femur, tibia, clavicle and lumbar vertebra under different test conditions. The bone fractures were assessed by both, the localized stress-strain characteristics as well as the global force-deflection responses. This analysis indicates that the maximum Von-Mises stress (MVMS) should be a good injury indicator for the bones with high cortical indices, independent of load directions. For the vertebral bodies with very low cortical index (1-3%), the ultimate strain of the trabecular bone may be considered as indicator for the bone fractures.

INTRODUCTION

Occupant injury assessment tools are essential to research and development of advanced occupant restraint systems. Traditionally, Anthropomorphic Test Devices (ATDs) have been used in laboratories to evaluate the restraint system performance. In recent years human body models have been developed as an important tool to help assess restrained occupant injuries which could not be evaluated by the ATDs due to their biofidelic deficiencies. The human body finite element model for an average adult male reported earlier [1], was one such tool for injury analyses of the thorax, abdomen and shoulder of a belted occupant. However, this model was not fully biofidelic and thus needed to be further developed.

A biofidelic full human body model requires two essential elements: the anatomical structures and the material characterization of human. All the human (hard and soft) tissues of which injuries were observed in field should be modeled in the anthropometrical details and their physical material properties should be investigated.

As an applicable occupant injury assessment tool the human model was required to be fully validated for its biofidelity. Such validations, as per Yang et al. [2], should be carried out against the cadaveric or human volunteer tests data in a variety of impact conditions such as frontal, side, rear, and oblique for all the body regions at three levels: the component (tissue), the subsystem (body part), and the system (whole-body), to ensure their predictive accuracy for human responses and computation robustness.

Human hard tissues are those that have become mineralized, or having a firm intercellular substance, e.g., cartilage and bone. The human model should have predictive capabilities for their fractures. Although great efforts have been made so far to develop the modeling techniques and fracture prediction capabilities for such human bony parts as skull [3], cervical spine [4], thoracic ribs [5], bones of the pelvis and the lower limb [6], the injury measures and thresholds in terms of strain or stress at the local tissue level were still not well established, and the co-relationship between the injury measures and tolerances in terms of measurable global indicators and those in terms of local strain or stress were not fully understood.

From the existing biomechanical research results we knew that two kinds of human bones—the trabecular and the cortical have much different microstructures, material properties and strengths. The modulus of the

cortical bones can be 100-1000 times higher than that of the trabecular bones. The stiffness, strength and tolerance of a piece of bone are dependent on the cortical index which is the combined cortical thickness divided by the thickness of the bone. The thickness of the cortical shell, again, varies from bone to bone, region to region, and even varies with age and gender. For example, the shafts of femur and tibia have the cortical index of 1, on the other hand, the lumbar vertebral bodies (L1-L5) have average cortical thickness of only 0.3mm (or about 1% of cortical index) [7]. In between, the clavicle cortical index decreases from 0.6 at 25 years-old to about 0.38 at 80 years-old for female, and from 0.5 at 25 years-old to about 0.3 at 80 years-old for male [8]. Studying these bones whose cortical indices vary from 0.01 to 1 could help us understand better the fracture mechanisms and tolerances of the human hard tissues.

This research pursued the following objectives:

1. to construct a full human body model including the anatomical details of skeleton and major soft tissues in all the body parts (head, neck, shoulder, thorax, abdomen, pelvis, lower and upper extremities); and to complete full validations on the model's biofidelity at the component, subsystem and system levels under various loading/impact conditions;

2. using the model to analyze the fracture mechanisms and tolerances of femur, tibia, clavicle and lumbar vertebra in terms of both global measures and local strain or stress in order to better understand injury mechanisms and tolerances of the human hard tissues.

CONSTRUCTION OF A BIOFIDELIC MODEL

Great efforts have been made to update the earlier version of the 50th% male human model [1] to a full biofidelic model. The completed development work can be explained in three sections: the anatomical modeling, the tissue material modeling, and the model biofidelity validation.

Anatomical Modeling

Additional modeling work for the anatomical structures in all the following body regions is described briefly below.

The Head - The skull, modeled in three layers (inner, diploe, outer) in solid elements, was partitioned as multiple zones representing bones of

Frontal, Parietal, Occipital, Temporal, Sphenoid, Maxilla+Ethmoid, and Mandible. The finer element sizes of the average 2.5mm were meshed in the whole brain region. Currently, the Cerebrospinal fluid (CSF) was modeled in three layers of solid elements materialized with the fluid-like behavior defined by LSDYNA MAT_ELASTIC_FLUID material type. However, different modeling methods are being explored for local failure estimations.

The Neck - The occipital condyle was modeled, adding more ligaments and membranes (Alar, Cruciate, Alantooccipital, Tectorial, Apical). The Capsule of zygapophyseal joints between C2-3, C3-4, C4-5, C5-6, C6-7 were defined as combination of solids contact interfaces and 2D membrane ligaments. Five cervical ligaments (anterior longitudinal, posterior longitudinal, joint capsules, ligamentum flavum, interspinous) were modeled as 2D membrane elements. Ten pairs of neck muscles (Sternocleidomastiod, Sternothyroid, Sternohyoid, Thyrohyoid, Omohyoid, Trapezius, Scalene, Splenius, Levator scapulae, Platysma) were modeled as combination of solids and 1D Discrete element with the LSDYNA Hill-type muscle material model.

The Thorax - The original rib cage model was divided into anterior, lateral, and posterior segments as the same defined by Stitzel et al. [9] to take into account of the regional variation of stiffness and strength of the rib cortical bone.

The Shoulder – The clavicle bones were re-modeled in the finer mesh sizes of average 1.2 mm to better predict the fracture. All the ligaments, tendons, and muscles connecting the Clavicle, Sternum and Ribcage, Acromion, Scapula and Humerus were thus re-meshed to ensure integrity of the whole shoulder structures.

The Abdomen – The lower abdomen were reconstructed to adapt to the updated pelvis. The abdominal aorta and inferior vena cava were modeled.

The Pelvis and The Upper and Lower Extremities – New full finite-element sub-models for the pelvis, the lower extremities and the upper extremities were constructed. The anthropometrical data of all the bony parts in these three body regions were obtained from two resources: 1) the full-color cross-section image data of the Visible Human Male Subject segmented by in-house 3D-Doctor software; or 2) the MRI male subject data from Wayne State University. Additional tissues segmented by using

the 3D-Doctor and meshed by using Hypermesh included the Sciatic nerves coming from the lower spines (L4-5, S1-3) through its Common fibula division and Tibial nerve in the thigh and knee regions, the main arteries of thigh and knee (External Iliac, Femoral, Deep, Anterior and Posterior Tibial), and all the knee ligaments (ACL, PCL, MCL, LCL). All the segmented data were scaled to 50th% male size based on the UMTRI data.

The hard tissues modeled in the pelvis region included lumbar, sacrum and coccyx, ilium, ischium, pubis, symphisis pubica, and acetabulum. The sacroiliac joint was modeled as tied surfaces. The hip joints were modeled as combination of the hip joints ligaments (ligament of femur head, the capsular ligaments), the synovial membranes and contact between the femur head and acetabulum. The pelvis bones were directly connected to lower abdomen hollow organs, fats and outer skins. Two joints in each of the knee were carefully modeled: the femoro-patellar joint consisting of the patella, patellar and quadriceps tendons, and the patellar groove; the femoro-tibial joint consisting of the femur condyle and articular cartilage, the tibia and fibula and meniscus, as well as the ligaments of ACL, PCL, MCL, LCL. The synovial membranes were modeled as surfaces for soft contacts.

All pieces of bones and major ligaments in the body regions of lower leg, ankle/foot, upper and lower arms and elbow, wrist and hands were modeled. The cortical bones in the shaft of the long bones (femur, tibia and fibula) were modeled as solid elements, and those in the head/condyle region were modeled as shells with varying regional thickness measured by using 3D-Doctor software or from the literature. All the trabecular bones were modeled in solid elements.

Along their routes, the branches of the main arteries/nerves were modeled as discrete spring elements, and the connections among these nerves/arteries and their surrounding muscles were modeled with the method of tied nodes. The skins and muscles of the lower limb were meshed as solid elements which were tied with the bony structures.

The updated human model is fully deformable representing an average adult male with weight of 77.8Kg. It consists of 154,142 elements, 113,349 nodes, and 701 components for the tissues. Figure 1 shows this model.
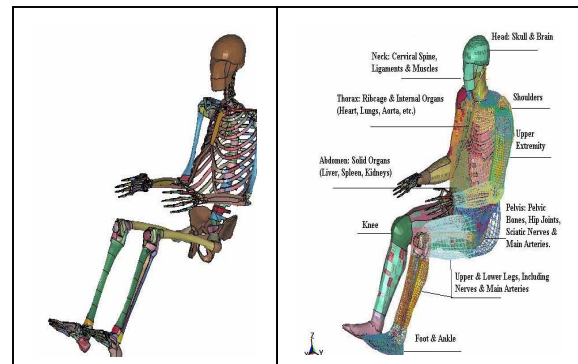

Figure 1. The updated Takata Human Model. Left-Skeleton; Right-Full body.

Tissue Material Modeling

There are 589 material cards in total with sixteen material models (constitutive laws) defined in this updated human body model. Table 1 summarizes the material models used for the tissue components.

Table 1 The Material Models and Cards in the Model

Material Model	Tissues	Total
01-Elastic	The connective tissues being not easily injured	275
01-Elastic Fluid	CSF	1
03-Plastic Kinematic	Other connective tissues	37
06-Viscoelastic	Brain, abdominal solid organs	13
09-Null	Internal contact interfaces	7
20-Rigid	Local coordinate base	1
24-PiecewiseLinearPlasticity	Ligaments, tendons	133
34-Fabric	Capsule membranes	6
57-LowDensityFoam	Hollow organ inserts	3
62-ViscousFoam	Skin, body fats	18
81-PlasticitywithDamage	Cortical bones	28
105-Damge 2	Trabecular bones, cartilages	37
129-LungTissue	Lungs, heart	2
SB1-Seatbelt	Tendons	13
DS4-SpringNonlinearElastic	Artery branches	5
DS15-SpringMuscle	Neck Muscles	10
ALL	--	589

The material properties or parameters in the material models were determined in three ways: 1) directly from the published tissue material tests data; 2) from our tissue test component model correlations; and 3) from our body impact subsystem model correlations.

The directly applied tissue material property data were selected from the cadaver or live porcine tissue coupon tests. Examples of such coupon tests were for the rib cortical shells [9], the cervical and lumbar

spine ligaments [10, 11], the scalp and brain tissues and the skull (inner and outer tables and diploe) [12], the shoulder ligaments of OC, CC, SC joints [13], the auricular and costal Cartilage [14], and the cortical shells of Femur, Tibia, Fibula, Humerus, Radius, and Ulna [15], etc.

However, quite a few biomechanical tests were performed at the tissue component (consisted of a group of tissues) level. In addition, the existing published tissue material property data, especially of the soft tissues, varied in wide range due to different subjects, test conditions and methods. Considered these uncertainties we selected the biomechanical tests for those tissues which were primary load carriers inside the body or easily sustained injuries. FE models for each of the test configurations were constructed and the test procedures were simulated. The model outputs defined according to the measurements were correlated with the test data. Through this process the material properties of these tissues were determined or estimated. Table A-1 in Appendix A lists all such simulated material tests in total of 20 that came from 10 studies involving 2 skull/brain tissue tests, 4 neck tissue tests, 4 thorax tissue tests, 3 abdomen organs tests, 1 clavicle tests, 4 lower extremity long bone tests, and 2 lumbar vertebra and disc tests. Table A-1 provides the information of the test conditions, the correlated responses and correlation quality grades (1-5, 1-unacceptable; 5-best; determined as explained in notes of Table A-1), and the references.

From the two ways described above, most of the tissue material properties defined in the model could be determined or estimated. For those of the modeled human tissues which were not tested in either coupon or component material tests, their material properties were estimated from the body impact subsystem model correlations.

Model Biofidelity Evaluation

Seven body regions (head, neck, shoulders including upper extremities, thorax, abdomen including lumbar, KTH, lower leg including ankle/foot) were validated against a set of the PMHS drop or pendulum and sled tests. These biomechanical tests included 47 in total from 22 studies that involved 5 head tests, 7 neck tests, 5 thorax tests, 5 abdomen tests, 5 shoulder tests, 5 KTH tests, 2 lower leg tests, 5 ankle tests, 6 lumbar tests, and 2 whole body sled tests. The selected tests data covered in a variety of impact energies and directions (frontal impacts-25; side/oblique impacts-16; rear impacts-3; axial-4).

The method for evaluation of biofidelity of the human model was similar to those defined in the ISO-TR9790 lateral biofidelity rating procedures [16]. The biofidelity rating calculation of each body region was defined by ISO as expressed in Eq. (1)

$$B_i = \frac{\sum_{j=1}^{m} V_{i,j} \left(\sum_{k=1}^{n} W_{i,j,k} R_{i,j,k} / \sum_{k=1}^{n} W_{i,j,k} \right)}{\sum_{j=1}^{m} V_{i,j}} \quad (1)$$

where $V_{i,j}$ were the weighting factor for each test condition for a given body region; $W_{i,j,k}$ were weighting factor for each response measurement for which requirement was given; $R_{i,j,k}$ were the rating of how well a given response meets its requirement. R=10 if response meets requirement; R=5 if response is outside requirement but lies within one corridor width of requirement; R=0 if neither of the above two is met. The overall rating for a given model was calculated via Eq. (2)

$$B = \frac{\sum_{i=1}^{7} U_i B_i}{\sum_{i=1}^{7} U_i} \quad (2)$$

where B was the overall rating which have a value between 0 (unacceptable) and 10 (excellent); B_i were the biofidelity rating of each of body regions; U_i were the weighting factors for the biofidelity rating of each of body regions.

To simply the rating calculation procedures we assigned all of the weighting factors $V_{i,j}$, $W_{i,j,k}$ and U_i equal to 1, which means that all the measured responses in each of the selected tests were equally treated, and that each of all the body regions were considered equally important.

All the test conditions, the measurements, the model's responses and the ratings $R_{i,j,k}$, as well as test data resource are summarized in Table A-2 and A-3 in Appendix-A. In Table A-3 the ratings of each response for a relevant body region were included in Eq.(1) while the external force measurements (marked NA in Table A-3) were excluded from the rating calculation. Table A-4 summarizes the biofidelity rating results for the body regions of the human model.

According to the ISO five biofidelity rating classifications, the biofidelity is considered as excellent if the rating scale is between 8.6[+]-10, and as good if the scale between 6.5[+]-8.6. The model achieved excellent biofidelity rating scores in the body region of Thorax (9.4). All the other body

regions (scored 7.2-8.6) achieved good biofidelity score. The overall biofidelity rating of the human model is good (8.1).

HARD TISSUE INJURY ANALYSIS

Based on the results of the bio-tests simulations listed in Table A-1, A-2, A-3, we summarize our findings from the hard tissue injury analysis particularly for femur, tibia, lumbar vertebra, and clavicle. The material properties of these bones in the sub-models are tabulated in Table B-1 in Appendix B.

Analysis of the 3-Point A-P Bending Tests on Femur and Tibia

In this study, static 3-point anterior-posterior (A-P) bending tests on femur and tibia were simulated. The model-predicted force-displacement curves of these bones were compared with the measured data [15], as shown in Figure 2.
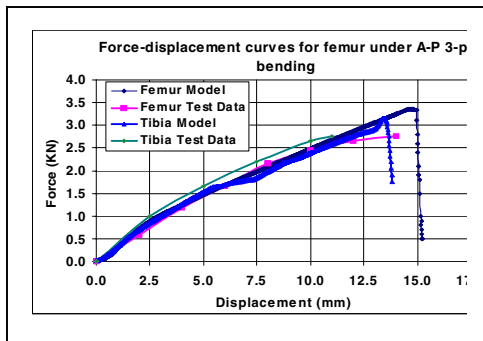

Figure 2. Comparison of the model predicted and the measured load force vs. displacement curves of the femur and tibia under quasi-static 3-point bending. The test data referred to [15].
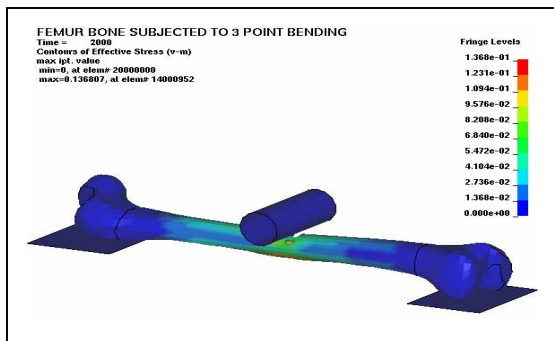

Figure 3. The stress contour of the femur under quasi-static 3-point bending at the failure time.

The simulations showed that corresponding to each of the peak forces in Figure 2 failure occurred in the shaft center of the femur or the tibia, where maximum stresses of the femur or tibia occurred as shown in Figures 3-4.
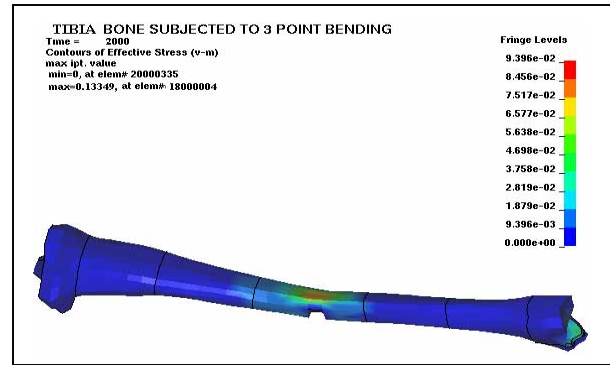

Figure 4. The stress contour of the tibia under quasi-static 3-point bending at the failure time.

Table 2 summarizes the calculated failure forces, maximum Von-Mises stresses and the failure strains of femur and tibia under the simulated A-P 3-point bending test conditions. It is noted here that in both cases the failure stresses are around 130MPa while the failure strains are around 1.3%.

Table 2 The calculated failure forces, stresses, and strains of the femur and the tibia

Tissue	Failure Force (KN)	Failure Stress (MPa)	Failure Strain (%)
Femur	3.3	136.8	1.4
Tibia	3.2	133.5	1.3

Analysis of the Compression Tests on the Lumbar Vertebrae

In this study, the compression tests on isolated lumbar vertebrae L1-L5 reported by Yoganandan et al. [17] were modeled. In the test set-up, a compressive load was uniformly applied to the vertebral body at a constant speed of 2.5 mm/s to about 50% of its original height. Figure 5 shows the model predicted force-deformation curve compared with the measured ones of L2, L3, L4 and L5 [17]. It was seen that the force-deformation curve of the vertebra had a plateau in which the large plastic deformation of the trabecular bone occurred.
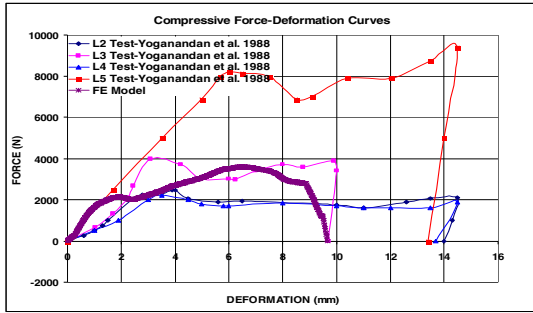
Figure 5: Comparison of the model predicted and measured force-deformation curves [17] of the lumbar vertebral bodies under quasi-static compressive loading.

Figure 6 shows that the maximum stresses were in the circumferential edge of the endplate where failure occurred.
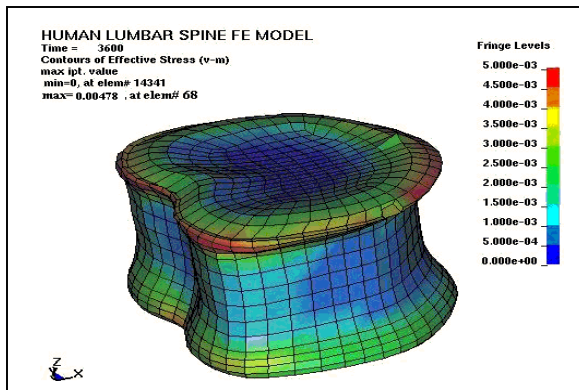

Figure 6. The stress contour of the lumbar vertebral body under quasi-static compressive loading at the failure time.

Table 3 summarizes the calculated failure force (the value when the force dropped significantly), maximum Von-Mises stresses of the vertebral bones and the failure strains of the trabecular bone under the compressive loading. It was interesting to see from the simulation that before the failure force a few percent of cortical and trabecular bone elements had already failed. The vertebral trabecular bone along carried about 70% of the total loads. Thus the failure stress and strain reflected dominantly the material characteristics of the trabecular bone.

Table 3 The calculated failure forces, stresses, and strains of the vertebra L3

Tissue	Failure Force (KN)	Trabecular Failure Stress (MPa)	Trabecular Failure Strain (%)	Cortical Failure Stress (MPa)
Vertebra L3	2.8	4.8	25.4	112.7

Clavicle Fracture Analysis

Clavicle three-point bending tests analysis

Quasi-static cadaver clavicle three-point bending tests were simulated. Table 4 compares the model outputs with the test results reported by Bolte et al. [43] and Probasta et al. [18].

Table 4 compares the model predicted maximum load force, stiffness, average failure stress and maximum deflection with the test data [18, 43].

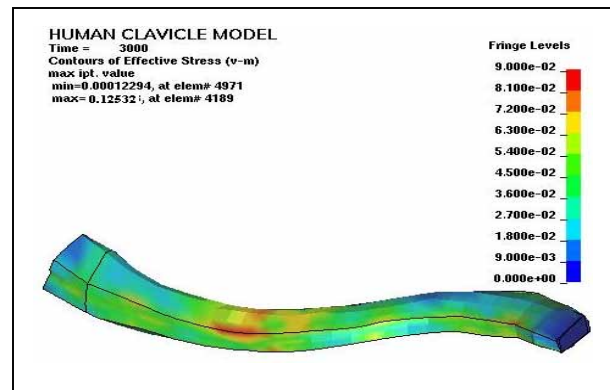| Source	Maximum Force (N)	Stiffness (N/mm)	Max. Deflection (mm)	Failure Stress (MPa)
Bolte's Average [43]	681.7	147.2	4.6	N/A
Proubasta's Average [18]	485.6	94.8	5.0	N/A
Model	529.9	99.6	5.3	125.0

Figure 7. The stress contour of the clavicle under 3-point bending.

Figure 7 shows the stress contour of the clavicle under 3-point bending at the failure moment. The clavicle fractured in the center of shaft body where the maximum Von-Mises stress was 125MPa.

Analysis of pendulum side impacts to shoulders

The tests of the pendulum side impacts to PMHS shoulders conducted by Bolte [43] and Compigne [19] were simulated. In Compigne's test set-ups, the PMHS were struck using a 23.4kg impactor fitted with a rigid rectangular shaped impacting plate in lateral and oblique (±15°) directions at different impact velocities (1.5-6 m/s). In Bolte's test set-ups, the left shoulder of PMHS was impacted with a 23 kg pneumatic ram (20cmX15cm, padded with a 5cm thick piece of Arcel foam) in lateral and oblique (15°, 30°) directions at impact speeds from about 4 to 7.5 m/s.

Figures 8-9 show the correlation of the model predicted acromion-to-sternum deflections and the

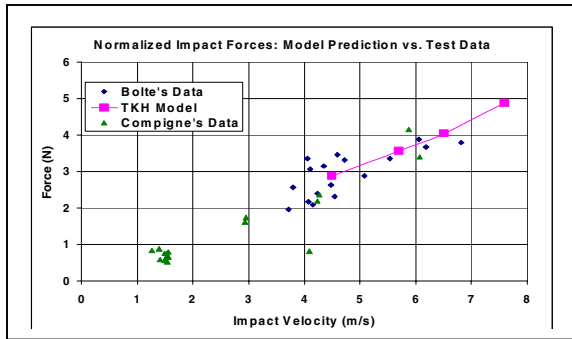impact forces with the Bolte's [43] and Compigne's test results [19].

Figure 8. Comparison of the model predicted Acromion-to-Sternum deflections varying with impact velocities with the test data [19, 43].
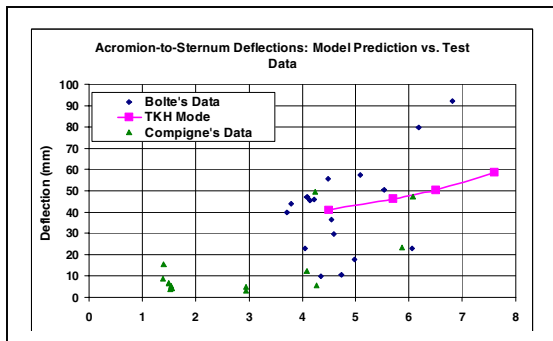

Figure 9. Comparison of the model predicted forces varying with impact velocities with the test data [19,43].

Table 5. Model Predicted Injury Numbers for PMHS Pendulum Side Impact Tests

Impact Velocity (m/s)	Max. Force (N)	Acr-To-Sternum Def. (Mm)	Max. Stress (MPa)
4.5	2.87	40.8	90.9
5.7	3.56	46.4	104.7
6.5	4.05	50.3	121.4
7.6	4.87	58.5	130.8

Table 5 correlates the maximum forces, the acromion-to-sternum deflections and the model-predicted maximum Von-Mises stresses of the clavicle responding to different pendulum impact speeds. At 6.5 m/s impact speed, the calculated acromion-to-sternum deflection was 50.3 mm while the maximum Von-Mises stress exceeded 120MPa, at which the bone fractured in the simulation. The past research concluded that under lateral impacts to PMHS shoulders 47 mm of the acromion-to-sternum deflection predicted a 50% probability of clavicle fracture or AIS 2+ shoulder injury. This study indicated that at failure the clavicle experienced the Von-Mises stress of more than 120 MPa.

DISCUSSION

In this study, all the investigated three bones (femur, tibia, clavicle) with high cortical indices (above 0.4) fractured consistently in the range of 120-130MPa of maximum Von-Mises stress (MVMS) of the cortical bones. This suggested that the MVMS can be a good injury indicator for these high cortical index bones, independent of load directions. The threshold of 120-130 MPa matched Stitzel's ultimate stress data from the rib cortical bone coupon tests [7].

For the vertebral bodies with very low cortical index (1-3%), the ultimate strain of the trabecular bone may be considered as indicator for the bone fractures.

More experimental studies are needed to confirm these analytical findings.

CONCLUSIONS

The updated Takata Human Model for an average adult male has the detailed bony and soft tissues in all the body regions. The overall biofidelity rating of the model is good (biofidelity rating score 8.1).

The results of simulated 3-point bending tests for the bones (femur, tibia, clavicle) with high cortical indices (0.4-1.0) showed that all of them fractured at 120-130MPa of the maximum Von-Mises stress (MVMS). Additional simulations for the lateral impacts to PMHS shoulders at different speeds of 4.5-7.6m/s concluded that 47 mm of the acromion-to-sternum deflection corresponded to 120MPa of the MVMS in the clavicle. All these results suggested that the MVMS be a good injury indicator for these high cortical index bones, independent of load directions.

The results of simulated compression tests on isolated lumbar vertebral body L3 with very low cortical index (~0.01) showed that the deformation pattern and fracture characteristics of the vertebral body were very similar to those of the trabecular bone of the body. The ultimate strain of the trabecular bone may be considered as indicator for fractures of the low cortical-index bones.

These analytical findings are worthy to be further investigated experimentally.

ACKNOWLEGEMENT

REFERENCES

[1] Jay Zhijian Zhao and Gopal Narwani, "Development of a Human Body Finite Element Model for Restraint System R&D Applications", 19th ESV Conference, Paper# 05-0399, 2005.

[2] Yang, K.H., Hu, J.W., White, N.A., King, A.I., Chou, C.C. and Prasad, P., "Development of Numerical Models for Injury Biomechanics Research: A Review of 50 Years of Publications in the Stapp car Crash Conference", Stapp Car Crash Journal, Vol. 50, 2006-22-0017, 2006.

[3] Ruan, J. and Prasad, P., "The Effects of Skull Thickness Variations on Human Head Dynamic Impact Responses", Stapp Car Crash Journal, Vol. 45, 2001-22-0018, 2001.

[4] Meyer, F., Bourdet, N., Deck, C., Willinger, R., Raul J.S., "Human Neck Finite Element Model Development and Validation against Original Experimental Data", Stapp Car Crash Journal, Vol. 48, 2004-22-0008, 2004.

[5] Tamura, A., Watanabe, I., Miki, K., "Elderly Human Thoracic FE Model Development and Validation", 19th ESV Conference, Paper# 05-0229, 2005.

[6] Untaroiu, C., Darvish, K., Crandall, J., Deng, B., Wang, J-T., "A Finite Element Model of the Lower Limb for Simulating Pedestrian Impacts", Stapp Car Crash Journal, Vol. 49, 2005-22-0008, 2005.

[7] Rotzel, H., Amling, M., Pösl, M., Hahn, M., Delling, G., "The Thickness of Human Vertebral Cortical Bone and Its Changes in Aging and Osteoporosis: A Histomorphometric Analysis of the Complete Spinal Column from Thirty-Seven Autopsy Specimens", J. Bone and Mineral Research, 12(1): 89-95, 1997.

[8] Helelä, T., "Age-dependent Variations of the Cortical Thickness of the Clavicle", Annals of Clinical Research, 1:140-143, 1969.

[9] Stitzel, J.D., Cormier, J.M., Barretta, J.T., Kennedy, E.A., Smith, E.P., Rath, A.L., Duma, S.M., "Defining Regional Variations in the Material Properties of Human Rib Cortical Bone and Its Effect on Fracture Prediction", Stapp Car Crash Journal, Vol. 47, 2003-22-0012, 2003.

[10] Yoganandan N., Pintar F. A., Kumaresan S., "Biomechanical Assessment of Human Cervical Spine Ligament", Stapp Car Crash Journal, Vol. 42, 983159, 1998.

[11] Pintar, F., Yoganandan, N., Meyers, T., Elhagediab, A., Sances Jr. A., "Biomechanical Properties of Human Lumbar Spine Ligaments", J. Biomechanics, 25(11):1351-1356, 1992.

[12] Melvin, J.W, McElhaney, J.H., Roberts, V.L., "Development of a Mechanical Model of the Human Head-Determination of Tissue Properties and Synthetic Substitute Materials", Stapp Car Crash Journal, Vol. 14, 700903, 1970.

[13] Koh, S.W., Cavanaugh J.M., and Leach J.P., Rouhana, S.W., "Mechanical Properties of the Shoulder Ligaments under Dynamic Loading", Stapp Car Crash Journal, Vol. 48, 2004-22-0006, 2004.

[14] Roy, R., Kohles, S.S., Zaporojan, V., Peretti, G.M., Randolph, M.A., Xu, J., Bonassar, L.J., "Analysis of Bending Behavior of Native and Engineered Auricular and Costal Cartilage", J. Biomedical Material Research, 68A: 597-602, 2004.

[15] Yamada, H., Strength of Biological Materials, Williams & Wilkins Inc., Baltimore, 1970.

[16] ISO-TR 9790, Road Vehicle Anthropomorphic Side Impact Dummy-Lateral Impact Response Requirements to Assess the Biofidelity of the Dummy, 1999.

[17] Yoganandan, N., Pintar, F., Sances, A. Jr., Maiman, D., Myklebust, J., Harris, G., Ray, G., "Biomechanical Investigations of the Human Thoracolumbar Spine", SAE Paper #881331, 1988.

[18] Proubasta, I.R., Itarte, J.P., Cáceres, E.P., Liusá, M.P., Gil, J.M, Planell, J.A.E., Ginebra, M.P.M., "Biomechanical Evaluation of Fixation of Clavicular Fractures", J. Southern Orthopaedic Association, 11(3):148-52, 2002.

[19] Compigne S., Caire, Y., Quesnel, T., Verriest, J-P., "Non-Injurious and Injurious Impact Response of the Human Shoulder Three-Dimensional Analysis of Kinematics and Determination of Injury Threshold", 48th Stapp Car Crash Conference, 2004-22-0005, 2004.

[20] Arbogast, K.B., Meaney, D.F., Thibault, L.E., "Biomechanical Characterization of the Constitutive Relationship for the Brainstem", Stapp Car Crash Journal, Vol. 39, #952716, 1995.

[21] Nightingale, R., Winkelstein, B.A., Knaub, K.E., Richardson, W.J., Luck, J.F., Myers, B.S., "Comparative Strengths and Structural Properties of the Upper and Lower Cervical Spine in Flexion and Extension", Journal of Biomechanics 35: 725-732, 2002.

[22] Yoganandan N. and Pintar F.A., "Biomechanics of Human Thoracic Ribs", Transactions of the ASME, Vol. 120, pp. 100-104, February 1998.

[23] Yen, M. R.T., "Development of Thorax Model Sub-project-C: Mechanical Properties of Human Heart, Lung and Aorta." Ph.D. Thesis of the Department of Biomedical Engineering of University of Memphis, September, 1999.

[24] Tamura, A., Omori K., Miki, K., Lee, J.B., Yang, K.H., King, A.I., "Mechanical Characterization of Porcine Abdomen Organs", Stapp Car Crash Journal, Vol. 46, 2002-22-0003, 2003.

[25] Keyak, J.H., Rossi, S.A., Jones, K.A., Skinner, H.B., "Prediction of Femoral Fracture Load Using Automated Finite Element Modeling", Journal of Biomechanics, 31:125-133, 1998.

[26] Gordon, S., Yang, K.H., Mayer, P., Mace, A., Kish, V., Radin. E., "Mechanism of Disc Rupture", Spine, 16(4): 450-456, 1991.

[27] Allsop, D.L., Warner, C.Y., Schneider. D.C., Nahum, A.M., "Facial Impact Response–A Comparison of the Hybrid III Dummy and Human Cadaver", Stapp Car Crash Journal, Vol. 32, 881719, 1988.

[28] Yoganandan, N. Zhang, J., Kuppa, S., Eppinger, R.H., "Biomechanics of Lateral Skull Fracture", IRCOBI Conference Proceedings, September 2003.

[29] Trosseille X., Tarriére, C., Lavaste, F., Guillon, F., Domont, A., "Development of a F.E.M. of the Human Head According to a Specific Test Protocol, Stapp Car Crash Journal, Vol. 36, 922527, 1992.

[30] Hardy, W.N., Foster, C.D., Mason, M.J., Yang, K.H., King, A., Tashman, S., "Investigation of Head Injury Mechanisms Using Neutral Density Technology and High-Speed Biplanar X-Ray", Stapp Car Crash Journal, Vol. 45, 2001-22-0016, 2001.

[31] Chris A. Van Ee, Nightingale, R.W., Camacho, D.L.A., Chancey, V.C., Knaub, K.E., Sun, E.A., Myers, B.S., "Tensile Properties of the Human Muscular and Ligamentous Cervical Spine", Stapp Car Crash Journal, Vol. 44, 2000-01-SC07, 2000.

[32] Pintar, F. A., Yoganandan N., Voo, L., Cusick, J.F., Maiman, D.J., Sances, Jr., A., "Dynamic Characteristics of the Human Cervical Spine", Stapp Car Crash Journal, Vol. 39, 952722, 1995.

[33] Thunnissen, J., Wismans, J., Ewing, C.L., Thomas, D.J., "Human Volunteer Head-Neck Response in Frontal Flexion: A New Analysis", Stapp Car Crash Journal, Vol. 39, 952721, 1995.

[34] Wismans J. and Spenny, C.H., "Performance Requirements for Mechanical Necks in Lateral Flexion", Stapp Car Crash Journal, Vol. 27, 831613, 1983.

[35] Viano, D.C., Hardy, W.N., King, A., "Response of the Head, Neck, and Torso to Pendulum Impacts on the Back", J. Crash Prevention and Injury Control, 2(4):289-306, 2001.

[36] Kroell, C. K., Schneider, D.C. and Nahum, A.M., "Impact Tolerance and Response of the Human Thorax", Stapp Car Crash Journal, Vol. 15, 710851, 1971.

[37] Kroell, C.K., Schneider, D.C. and Nahum, A.M., "Impact Tolerance and Response of the Human Thorax II." Stapp Car Crash Journal, Vol. 18, 741187, 1974.

[38] Viano, D.C., "Biomechanical Responses and Injuries in Blunt Lateral Impact." Stapp Car Crash Journal, Vol. 33, 892432, 1989.

[39] Kent R., Lessley, D., Sherwood, C., "Thoracic Response to Dynamic, Non-Impact Loading from a Hub, Distributed Belt, Diagonal Belt and Double Diagonal Belts." Stapp Car Crash Journal, Vol. 48, 2004-22-0022, 2004.

[40] Cavanaugh, J.M., Nyquist, G.W, Goldberg, S.J., King, A.I.,, "Lower Abdominal Tolerances and Responses." Stapp Car Crash Journal, Vol. 30, 861878, 1986.

[41] Hardy, W., Schneider, W. and Rouhana, S.W., "Abdominal impact Response to Rigid-Bar, Seatbelt, and Airbag Loading." Stapp Car Crash Journal, Vol. 45, 2001-22-0001, 2001.

[42] Bendjiella, F., Walfisch, G., Fayon, A., Tarriere, C., APR Biomechanical Data, Nanterre, France, 1984.

[43] Bolte IV, J.H., Hines, M.H., Herriot, R.G., McFadden, J.D., and Donnelly, B.R., "Shoulder

Impact Response and Injury Due to Lateral and Oblique Loading." Stapp Car Crash Journal, Vol. 47, 2003-22-0003, 2003.

[44] Guillemot, H., Got, C., Besnault, B., Coz, J.Y.L., Robin, S., Lavaste, F., Lassau, J.-P., "Pelvic Injuries in Side Impact Collisions: A Filed Accident Analysis and Dynamic Tests on Isolated Pelvic Bones", 41st Stapp Car Crash Journal, Vol. 41, 973322, 1997.

[45] Rupp, J.D., Reed, M.P., Van Er, C.A., Kuppa, S., Wang, S.C., Goulet, J.A., Schneider, L.W., "The Tolerance of the Human Hip to Dynamic Knee Loading", Stapp Car Crash Journal, Vol. 46, 2002-22-0011, 2002.

[46] Haut, R.C., Atkinson, P.J., "Insult to the Human Cadaver Patellofemoral Joint: Effects of Age on Fracture Tolerance and Occult Injury", Stapp Car Crash Journal, Vol. 39, 952729, 1995.

[47] Hayashi, S., Choi, H.-Y., Levine, R.S., Yang, K.H., King, A.I., "Experimental and Analytical Study of Knee Fracture Mechanisms in a Frontal Knee Impact", Stapp Car Crash Journal, Vol. 40, 962423, 1996.

[48] Dhaliwal, T.S., Beillas, P., Chou, C.C. Prasad, P., Yang, K.H., King, A.I., "Structural Response of Lower Leg Muscles in Compression: A Low Impact Energy Study Employing Volunteers, Cadavers and the Hybrid III", Stapp Car Crash Journal, Vol. 46 2002-22-0012, 2002.

[49] Crandal, J.R., Portier, L., Petit., P., Hall, G.W., Bass, C.R., Klopp, G.S., Hurwitz, S., Pilkey, W.D., Trosseille, X., Tarrière, C., Lassau, J.-P., "Biomechanical Response and Physical Properties of the Leg, Foot and Ankle", Stapp Car Crash Journal, Vol. 40, 962424, 1996.

[50] Rudd, R., Crandall, J., Millington, S., Hurwitz, S., Höglund, N., "Injury Tolerance and Response of the Ankle Joint in Dynamic Dorsiflexion", Car Crash Journal, Vol. 48, 2004-22-0001, 2004.

[51] Forman, J., Lessley, D., Kent, R., Bostrom, O., Pipkorn, B., "Whole-body Kinematic and Dynamic Response of Restrained PMHS in Frontal Sled Tests", Stapp Car Crash Journal, Vol. 50, 2006-22-0013, 2006.

APPENDIX A   Results of Material Modeling and Biofidelity Evaluation of the Takata Human Model

Table A-1 Summary of the bio-tissue test simulations for determining the material properties

Body Region	Tissue	Test conditions	Correlated Responses	Correlation quality*	Ref
Head	Cerebrum, Brainstem	Oscillating shear test over 20-100Hz and stress relaxation test at 7.5%	Stress-strain curve and Stress relaxation curve	4	[20]
Neck	OC-C1-C2 FSU	Quasi-static flexion and extension loadings.	Moment My vs. Rotation angle measure at C2.	4	[21]
Neck	C5-C6 FSU	Quasi-static flexion and extension loadings.	Moment My vs. Rotation angle measure at C6.	4	[21]
Thorax	Rib	3-point bending at quasi-static rate of 2.5 mm/min.	Max. load and deflection	4	[22]
Thorax	Heart	Biaxial tensile tests for cadaver heart samples	Average stress-strain curve	5	[23]
Thorax	Aorta	Biaxial tensile tests for cadaver aorta samples	Average Stress-strain curve	4	[23]
Thorax	Lungs	Biaxial tensile tests for cadaver lung samples	Average Stress-strain curve	5	[23]
Abdomen	Liver	Uniaxial compression to porcine liver at three loading rates *0.001/s, 0.05/s, 0.5/s)	Average Stress-strain curve	5	[24]
Abdomen	Kidney	Uniaxial compression to porcine kidney at three loading rates *0.001/s, 0.05/s, 0.5/s)	Average Stress-strain curve	5	[24]
Abdomen	Spleen	Uniaxial compression to porcine spleen at three loading rates *0.001/s, 0.05/s, 0.5/s)	Average Stress-strain curve	5	[24]
Shoulder	Clavicle	3pt bending tests at 0.5 mm/sec	Stiffness and failure load	5	[18, 43]
KTH	Femur Shaft	Quasi-static 3-pt bending tests	Load force vs. Deflection curve	5	[15]
KTH	Femoral head	Quasi-static loading to femoral head.	failure load	3	[25]
Lower Leg	Tibia & Fibula	Quasi-static 3-pt bending tests	Load force vs. Deflection curve	5	[15]
Lumbar Spine	Vertebra	Compressive loading at 2.5 mm/sec	Load force vs. Deformation curve	4	[17]
Lumbar Spine	Disc	Quasi-static compressive loading cyclically at 15.Hz up to 3mm.	Stiffness	4	[26]

* The correlation quality grades (1-5) are defined as follows: 1-unacceptable: the peaks and phases of the two curves behaviors totally different. 2-poor: the peaks and phases of the two curves do not match but trends are similar. 3-fair: both peaks and phases of the two curves differ within the range of 30%. 4-good: both peaks and phases of the two curves differ within the range of 20%. 5-excellent: both peaks and phases of the two curves differ within the range of 10%.

Table A-2 Summary of the PMHS drop or pendulum tests and biofidelity rating results for the body regions

Body region	Impact direction	Test conditions	Response	Requirement	Results	Rating	Ref.
Head	F	14.5kg 20mm rod impact to frontal bone at drop height of 460-915mm.	Force-Deformation curves	(2.5KN, 5.5KN) at 5 mm deformation	5.4 KN at 5mm	10	[27]
Head	F	14.5kg 20mm rod impact to Zygoma bone at drop height of 305-610 mm.	Force-Deformation curves	(1.4kN, 2.0KN) at 20mm	1.9KN at 20mm	10	[27]
Head	F	14.5kg 20mm rod impact to Maxilla bone at drop height of 305-610 mm.	Force-Deformation curves	(0.8KN, 1.8KN) at 20mm;	1.3KN at 20mm	10	[27]
Head	L	Head drop laterally to a 40-durometer padding place (50mm-thickness) at 6.5 m/s	Average peak force and displacement	Force: 8.4±1.4KN; Displ: 15.0±2.3mm	7.9KN, 16.4mm	10	[28]
Head	F	A rod impact to face in the antero-posterior direction at 7m/s. Test#MS428-2.	Intracranial pressures: Frontal	87KPa at 11ms	91.7 KPa at 10ms	10	[29]
Head	F	A rod impact to face in the antero-posterior direction at 7m/s. Test#MS428-2.	Intracranial pressures: Occipital	-11.4KPa at 9ms	-13.4KPa at 9ms	5	[29]
Head	F	A rod impact to face in the antero-posterior direction at 7m/s. Test#MS428-2.	Intracranial pressures: Lateral	39.8KP at 11ms	40.5KPa at 10ms	10	[29]
Head	F	A rod impact to face in the antero-posterior direction at 7m/s. Test#MS428-2.	Intracranial pressures: 3rd Ventricle.	30KPa at 10ms	27.8KPa at 10ms	10	[29]
Head	F	Suspended Head accelerated and impacted to a padded linear-piston impostor at 2 m/s. Test#C755-T2:	Brain targets X-Z displacements at sagittal plane	Figure 6 in [26]	maximum difference 28%	0	[30]
Neck	A	Eccentricity tensile loading to cervical spine at 2mm/s at free cranial end condition	Force vs Displacement	225KN at 7.5 mm	270KN at 7.5mm	5	[31]
Neck	A	Compressive loading to cervical spine by a padded plate at 2.5 m/s.	Force-deformation	Force-deformation corridor in Figure 6 [32]	Stay in between the corridors	10	[32]
Neck	F	Analyzed test data of head-neck to T1 relative motion responding to the 15.6G frontal sled pulse.	Head CG to T1 relative displacements X,Z	Head X (140mm,165mm) Head Z (200mm,225mm)	Head X 190 mm Head Z 235 mm	5	[33]
Neck	L	Analyzed test data of head-neck to T1 relative motion responding to the 7g lateral sled pulses.	Head CG to T1 relative displacements Y,Z	Head Y (120mm,141mm) Head Z (60mm,90mm)	Head Y 120 mm Head Z 51 mm	10	[34]
Neck	R	23.4 kg 150mm disk impact to rear skin at the level of T1 at 4.4 m/s.	Impact force history	(2.5KN, 3.8KN) in 8.5-10.0 ms	3.7KN at 13mm	5	[35]
Neck	R	23.4 kg 150mm disk impact to rear skin at the level of T1 at 4.4 m/s.	Head CG X-displacement	(125mm, 200mm) at 120ms	195mm at 120ms	10	[35]
Neck	R	23.4 kg 150mm disk impact to rear skin at the level of T1 at 4.4 m/s.	Head CG Z-displacement	(-24mm,45mm) at 120ms	35mm at 120ms	10	[35]
Neck	R	23.4 kg 150mm disk impact to rear skin at the level of T1 at 4.4 m/s.	Head rotation	(15deg, 65deg) at 120ms	31deg at 120ms	10	[35]
Neck	R	23.4 kg 150mm disk impact to rear skin at the level of T1 at 6.6 m/s.	Impact force history	(4KN, 6KN) at 10ms	5.8KN at 13ms	5	[35]
Neck	R	23.4 kg 150mm disk impact to rear skin at the level of T1 at 6.6 m/s.	Head CG X-displacement	(80mm, 280mm) at 80ms	160mm at 80ms	10	[35]
Neck	R	23.4 kg 150mm disk impact to rear skin at the level of T1 at 6.6 m/s.	Head CG Z-displacement	(-35mm,30mm) at 70ms	65mm at 70ms	0	[35]
Neck	R	23.4 kg 150mm disk impact to rear skin at the level of T1 at 6.6 m/s.	Head rotation	(20deg, 75deg) at 120ms	33deg at 80ms	10	[35]
Thorax	F	23.4kg 152mm disk at 6.5 m/s to center of thorax	Force-Deflection curve	Corridor	4.17KN at 72.1mm.	10	[36, 37]
Thorax	L	23.4kg 152mm disk at 30 degree oblique at 6.7 m/s to left side of thorax	Force-Deflection curve	Corridor	2.93KN at 73.3mm.	10	[38]
Thorax	F	UVA hub loading to thorax	Force-Deflection curve	Corridor	2.3KN at 65mm.	10	[39]

Thorax	F	UVA diagonal belt loading to thorax	Force-Deflection curve	Corridor	2.1KN at 37mm.	10	[39]
Thorax	F	UVA distributed loading to thorax	Force-Deflection curve	Corridor	4.1KN at 56mm.	10	[39]
Abdomen	F	32 kg bar at 6.1 m/s to lower abdomen.	Force-Deflection curve	Corridor: (2.16KN,4.2KN) at 120mm	4.5KN at 120mm	5	[40]
Abdomen	F	48kg rigid bar rigid-bar test at 9 m/s to free back cadavers	Force-Deflection curve	Corridor: (7KN,11.5KN) at 140mm	9.7KN at 137mm	10	[41]
Abdomen	L	23.4 kg disk at 30 degree oblique at 6.5 m/s to right side of upper abdomen.	Force-Deflection curve	Corridor: (3KN,4.5KN) at 100mm	5KN at 98.4mm	5	[38]
Abdomen	F	Close proximity surrogate airbag loading to midabdomen of fixed-back cadaver.	Force-penetration curve	Corridor: (2.5KN, 5KN) at 10mm	3KN at 10mm	10	[41]
Abdomen	F	Seat belt loading at 3.2m/s maximum to midabdomen of free-back cadaver.	Force-penetration curve	Corridor: (3.5KN, 4.4KN) at 50mm	3.8KN at 48.3mm	10	[41]
Shoulder	F	23 kg 150mm disk impact to left shoulder at 4.5 m/s.	Force-time history	Corridor: (1.6KN, 2.7KN) at 11ms	1.8KN at 11ms	10	[42]
Shoulder	L	23 kg 200X1500mm ram impact to left shoulder at 4.4 m/s.	Force vs Acromion-Acromion Deflection	Corridor: (2.1KN, 2.8KN) at 25mm	2.1KN at 25mm	10	[43]
Shoulder	O	23 kg 200X1500mm ram 15-Deg oblique impact to left shoulder at 4.4 m/s.	Y-Force vs Acromion-Acromion Y-Deflection	Corridor: (1.1KN, 1.7KN) at 15mm	1.8at 15mm	5	[43]
Shoulder	O	23 kg 200X1500mm ram 15-Deg oblique impact to left shoulder at 4.4 m/s.	X-Force vs Acromion-Acromion X-Deflection	Corridor: (0.4KN, 0.6KN) at 27mm	0.35KN at 27mm	5	[43]
Shoulder	O	23 kg 200X1500mm ram 30-Deg oblique impact to left shoulder at 4.4 m/s.	Y-Force vs Acromion-Acromion Y-Deflection	Corridor: (1.28KN, 1.44KN) at 15mm	1.56at 15mm	5	[43]
Shoulder	O	23 kg 200X1500mm ram 30-Deg oblique impact to left shoulder at 7.6 m/s.	X-Force vs Acromion-Acromion X-Deflection	Corridor: (0.79KN, 0.92KN) at 50mm	0.67KN at 50mm	5	[43]
KTH/Pelvis	L	23.4 kg rigid pendulum impact at 5.2m/s laterally to pelvis of seated cadavers.	Force-Deflection curve	Corridor: (5KN,8KN) at 40mm	4.6KN at40mm	10	[38]
KTH/Pelvis	L	23.4 kg rigid pendulum impact at 9.8m/s laterally to pelvis of seated cadavers.	Force-Deflection curve	Corridor: (10KN,15KN) at 50mm	17KN at 50mm	5	[38]
KTH/Pelvis	L	3.4 kg rigid ball impact to the acetabulum of isolated cadaver pelvic bones at 4 m/s.	Force-time history	Corridor: (1.7KN, 3.5KN) at 2.5ms	2.2KN at 2.5ms	10	[44]
KTH/Pelvis	F	270kg padded pendulum impact to KTH complex at 1.2m/s.	Force-time history	Corridor: (4KN, 10KN) at 30ms	6.6KN at 30ms	10	[45]
KTH/Knee	F	4.5 kg rigid pendulum impact to isolated knee with 6 different velocities from 1-6m/s.	Max. Force vs. Impact energy	2KN at 3J; 8KN at 61J	2.3KN at 3J; 8.2KN at 61J	10	[46, 47]
LLF/Lower leg	L	1.84 kg 145X45mm bar impact laterally to the lower leg below knee at 2.56 m/s.	Max Force & Penetration	5.96 KN at 22 mm	5.88KN at 19mm	10	[48]
LLF/Lower leg	R	1.72 kg 145X45mm bar posterior-anterior impact the lower leg at 2.56 m/s.	Max Force & Penetration	0.48 KN at 34mm	0.45KN at 28mm	5	[48]
LLF/Ankle	F	Quasi-static dosiflexion loading to ankle.	Moment vs Angle curve	69 N-m at 45deg	68N-m at 45deg	10	[49,50]
LLF/Ankle	F	Quasi-static plantarflexion loading to ankle.	Moment vs Angle curve	37 N-m at 65deg	39N-m at 65deg	10	[49]
LLF/Ankle	L	Quasi-static Inversion loading to ankle.	Moment vs Angle curve	12 N-m at 45deg	13 N-m at 45deg	10	[49]
LLF/Ankle	L	Quasi-static Eversion loading to ankle.	Moment vs Angle curve	40 N-m at 40deg	33 N-m at 40deg	5	[49]
ABD/Lumbar	A	Quasi-static compressive loading to lumbar spine at 8mm/s.	Z-Force-Displacement corridor	(0.4KN,1.5KN) at 3mm	0.9KN at 3mm	10	**
ABD/Lumbar	A	Quasi-static tensile loading to lumbar spine at 8mm/s.	Z-Force-Displacement corridor	(0.08KN,0.22KN) at 2 mm	0.26Kn at 2 mm	5	**

Zhao13

ABD/Lumbar	F	Quasi-static anterior shear loading to lumbar spine at 4mm/s.	X-Force-Displacement corridor	(0.1KN,0.37KN) at 10mm	0.18KN at 10mm	10	**
ABD/Lumbar	F	Quasi-static posterior shear loading to lumbar spine at 4mm/s.	X-Force-Displacement corridor	(0.15KN,0.5KN) at 10mm	0.22KN at 10mm	10	**
ABD/Lumbar	F	Quasi-static flexion loading to lumbar spine at 5deg/s.	y-Moment vs Angle corridor	(30NM,80NM) at 6 deg	37NM at 6deg	10	**
ABD/Lumbar	F	Quasi-static extension loading to lumbar spine at 5deg/s.	y-Moment vs Angle corridor	(20NM,75NM) at 6 deg	33NM at 6deg	10	**

* KTH--Knee Thigh & Hip; LLF--Lower Leg & Foot; ABD—Abdomen.

** In-house data

Table A-3 Summary of the PMHS sled tests and biofidelity rating results for the whole body

Test conditions	Response measurement	Test Results	Model	Body Region	Rating	Ref.
Driver case[1]	Upper Shoulder belt force	(3.59KN,4.24KN)	3.58KN	NA	**10**	[51]
Driver case[1]	Lower Shoulder belt force	(2.39KN,2.65KN)	2.49KN	NA	**10**	[51]
Driver case[1]	Lap belt force	(1.72KN,2.18KN)	1.67KN	NA	**5**	[51]
Driver case[1]	Left Knee bolster force	(1.84KN,3.42KN)	3.2KN	NA	**10**	[51]
Driver case[1]	Right Knee bolster force	(1.6KN,3.3KN)	3.6KN	NA	**10**	[51]
Driver case[1]	Head CG X-displacement	(254mm,325mm)	335 mm	Head	**10**	[51]
Driver case[1]	Head CG Z-displacement	(45mm,60mm)	64 mm	Head	**5**	[51]
Driver case[1]	Shoulder X-displacement	(164mm,278mm)	242mm	Shoulder	**10**	[51]
Driver case[1]	Shoulder Z-displacement	(-8 mm,-24 mm)	-40mm	Shoulder	**5**	[51]
Driver case[1]	Pelvis CG X-displacement	(65mm,158mm)	88mm	KTH	**10**	[51]
Driver case[1]	Pelvis CG Z-displacement	(64mm,66mm)	46 mm	KTH	**5**	[51]
Driver case[1]	Knee X-displacement	(20mm,54.3 mm)	64 mm	KTH	**5**	[51]
Driver case[1]	Knee Z-displacement	(38 mm,85mm)	32 mm	KTH	**5**	[51]
Driver case[1]	Chest Deflection from Upper chest band	(40 mm,60mm)	33 mm	Thorax	**10**	[51]
Driver case[1]	Right Rib8 compression from Lower chest band	(12.5 mm,55mm)	21 mm	Thorax	**10**	[51]
Passenger case[2]	Upper Shoulder belt force	(2.9KN,4.5KN)	3.88KN	NA	**10**	[51]
Passenger case[2]	Lower Shoulder belt force	(2.1KN,2.65KN)	2.5KN	NA	**10**	[51]
Passenger case[2]	Lap belt force	(1.83KN,2.04KN)	1.87 KN	NA	**10**	[51]
Passenger case[2]	Head CG X-displacement	(254mm,329mm)	335 mm	Head	**10**	[51]
Passenger case[2]	Head CG Z-displacement	(225 mm,267 mm)	200 mm	Head	**5**	[51]
Passenger case[2]	Shoulder X-displacement	(115mm,230mm)	180 mm	Shoulder	**10**	[51]
Passenger case[2]	Shoulder Z-displacement	(-60mm,100mm)	-25 mm	Shoulder	**10**	[51]
Passenger case[2]	Pelvis CG X-displacement	(-25 mm, 60mm)	75 mm	KTH	**5**	[51]
Passenger case[2]	Pelvis CG Z-displacement	(0mm,-18mm)	-21 mm	KTH	**5**	[51]
Passenger case[2]	Knee X-displacement	(-20 mm,60mm)	80 mm	KTH	**5**	[51]
Passenger case[2]	Knee Z-displacement	(30mm,80mm)	50 mm	KTH	**10**	[51]
Passenger case[2]	Chest Deflection from Upper chest band	42 mm	32 mm	Thorax	**5**	[51]
Passenger case[2]	Right Rib8 compression from Lower chest band	(17.5mm,40mm)	21.5 mm	Thorax	**10**	[51]

1--PMHS in a driver position, restrained with force limited 3 point belts plus airbag (FLB+AB), under 48 kmph mid-size sedan crash pulse

Zhao 14

2 -- PMHS in a passenger position, restrained with traditional (no force limit) 3 point belt (SB), under 29.8 kmph mid-size sedan crash pulse.

Table A-4 The biofidelity ratings of the Takata Human Model

Index	Body Region	Biofidelity Rating
1	Head	8.3
2	Neck	7.5
3	Shoulder	7.5
4	Thorax	9.4
5	Abdomen	8.6
6	KTH	7.3
7	Lower Leg	8.3
Overall		8.1

APPENDIX B

Table B-1 The Material Properties of the modeled femur, tibia, lumbar vertebra, and clavicle

Tissue	Material Model	Density(kg /mm^3)	E (GPa)	Poisson Ratio	Yield Stress (GPa)	Ep (GPa)	Failure Strain	Thickness (mm)
Clavicle cortical	24	2.00E-06	6.26	0.3	0.0626	4.78	0.0225	2.75
Clavicle trabecular	105	1.00E-06	0.010	0.35	0.002	0.005	0.22	--
Clavicle cartilage	24	1.10E-06	0.020706	0.45	0.0062	0.001		--
Lumbar vertebra trabecular	105	1.00E-06	0.02	0.3	0.00319	0.0	0.244	--
Lumbar vertebra cortical	81	1.41E-06	7.46	0.3	0.056	0.23	0.03	0.3
Femur shaft cortical	24	1.95E-06	17.6	0.315	0.088	4.8	0.014	5.0 (solid)
Femur condyle trabecular	105	1.00E-06	0.292	0.3	0.035	0.106	0.14	--
Femur condyle cortical	81	1.95E-06	17.6	0.315	0.0668	4.5	0.02	2-4 vary
Tibia shaft cortical	81	1.95E-06	20.3	0.315	0.0964	4.5	0.013	4.75 (solid)
Tibia condyle trabecular	105	1.00E-06	0.292	0.3	0.035	0.09	0.14	--
Tibia condyle cortical	81	1.95E-06	17.6	0.315	0.0668	4.5	0.02	2-4 vary